J. Fluid Mech. (1996), vol. 326, pp. 151–179

Interaction between a spatially growing turbulent boundary layer and embedded streamwise vortices

By JUNHUI LIU[1]†, UGO PIOMELLI[1] AND PHILIPPE R. SPALART[2]

[1]Department of Mechanical Engineering, University of Maryland, College Park, MD 20742, USA
[2]Boeing Commercial Airplane Group, PO Box 3707, Seattle, WA 98124-2207, USA

(Received 5 December 1995, and in revised form 20 May 1996)

The interaction between a zero-pressure-gradient turbulent boundary layer and a pair of strong, common-flow-down, streamwise vortices with a sizeable velocity deficit is studied by large-eddy simulation. The subgrid-scale stresses are modelled by a localized dynamic eddy-viscosity model. The results agree well with experimental data. The vortices drastically distort the boundary layer, and produce large spanwise variations of the skin friction. The Reynolds stresses are highly three-dimensional. High levels of kinetic energy are found both in the upwash region and in the vortex core. The two secondary shear stresses are significant in the vortex region, with magnitudes comparable to the primary one. Turbulent transport from the immediate upwash region is partly responsible for the high levels of turbulent kinetic energy in the vortex core; its effect on the primary stress $\langle u'v' \rangle$ is less significant. The mean velocity gradients play an important role in the generation of $\langle u'v' \rangle$ in all regions, while they are negligible in the generation of turbulent kinetic energy in the vortex core. The pressure–strain correlations are generally of opposite sign to the production terms except in the vortex core, where they have the same sign as the production term in the budget of $\langle u'v' \rangle$. The results highlight the limitations of the eddy-viscosity assumption (in a Reynolds-averaged context) for flows of this type, as well as the excessive diffusion predicted by typical turbulence models.

1. Introduction

Turbulent boundary layers with embedded streamwise vortices are an important type of three-dimensional wall-bounded flows, and are of great interest in engineering applications. Streamwise vortices are generated when any protuberance extends from a wall, or when fluid flows over a wall with streamwise curvature or through a non-circular channel. The streamwise vortices enhance heat and momentum transfer close to the wall, and are often introduced artificially by means of vortex generators to improve mixing and delay separation. However, under some circumstances, streamwise vortices can be undesirable; such is the case in gas turbines, where streamwise vortices increase the interaction between the hot gas stream and the cooled blades, severely damaging the blades. Since relatively weak vortices can have large effects on the

† Present address: Department of Aerospace Engineering and Mechanics, University of Minnesota, Minneapolis, MN 55455, USA.

surrounding flow, neglecting or mispredicting those effects could result in large errors in the engineering design. Many experiments have been conducted to improve our understanding and provide well-documented data for modelling and numerical simulation validation, notably at Imperial College and Stanford. Single vortices and vortex pairs, embedded in two- and three-dimensional boundary layers, were considered.

Mean-flow and turbulence quantities for an isolated vortex embedded in a low-speed turbulent boundary layer in zero pressure gradient were measured by Shabaka, Mehta & Bradshaw (1985). The magnitude of the secondary flow was approximately 5% of the free-stream velocity. They observed that the vortex circulation was almost conserved, and vorticity of opposite sign to the primary vorticity was found around the vortex. Negative Reynolds shear stress $-\langle u'v' \rangle$ (where $\langle \cdot \rangle$ represents averaging over time and a prime denotes a fluctuating quantity) was observed in the vortex core region. Spanwise profiles of the skin-friction coefficient showed both a rise and drop of 30% from the undisturbed flat-plate value. The effects of streamwise pressure gradient and heat transfer on the vortex development were studied by Westphal, Eaton & Pauley (1985) and Eibeck & Eaton (1985).

Mehta & Bradshaw (1988) and Pauley & Eaton (1988*a*, *b*) studied two counter-rotating vortices, denoted as a 'common-flow-up' vortex pair, in which the flow between the vortices is directed away from the wall. The vortices lifted from the wall, and reached a height of roughly twice the boundary-layer thickness, at which point they were connected by a tongue of upward-moving fluid, with a corresponding lateral convergence of boundary-layer fluid towards the plane of symmetry. This flow field was more complex than in the case of a single vortex. The contours of eddy viscosities and diffusivities were very ill-behaved, as were the contours of the bulk transport velocities of the Reynolds stresses.

The 'common-flow-down' vortex pair has been studied extensively by Pauley & Eaton (1988*a*, *b*) and Cutler & Bradshaw (1989). The vortices are held inside the boundary layer by their mutual interaction, and move apart downstream due to the image vortices. This type of vortex pair causes the greatest distortion of the boundary layer over the greatest streamwise distance; the boundary layer is thinned between the vortices and thickened in the regions where the secondary flow is directed away from wall. The vortex circulation decays much more slowly than the peak vorticity, but both of them decay faster than in the single-vortex case. The perturbation to the skin friction is much larger in the common-flow-down than in the common-flow-up case, and the Reynolds stresses present highly three-dimensional characteristics. Pauley & Eaton (1988*a*, *b*) observed that the heat transfer modification was strongly dependent on the vortex interaction and turbulent intensity near the wall.

Shizawa & Eaton (1992) studied the interaction between a single vortex and the pressure-driven three-dimensional boundary layer produced by a symmetrical 60° wedge placed downstream of a two-dimensional boundary layer. They observed that the turbulence development was very sensitive to the sign of the vortex. They also found that the peak vorticity and secondary velocities decay more rapidly than in a similar two-dimensional boundary layer.

Other experimental studies include Takagi & Sato (1983), Matsumoto (1986), Kim and Patel (1994), Wendt, Greber & Hingst (1992), and Fontaine, Bieniewski & Deutsch (1993). It was found that vortices with small vortex spacing remain in close proximity to the wall, and the resultant interaction with the boundary layer is strong; in addition, counter-rotating cores merge together as they develop downstream. The wall curvature has a strong effect on the interaction between the vortices and the

wall: the vortex circulation increases on a concave wall compared to a flat one. When a counter-rotating vortex pair is placed within the wall-layer region, a significant reduction in the primary Reynolds stress and turbulence production is observed.

Because of its simple geometry and three-dimensionality, the interaction between an otherwise two-dimensional turbulent boundary layer and embedded streamwise vortices has been also studied using the Reynolds-averaged Navier–Stokes equations. Reynolds-stress models originally developed for two-dimensional turbulent flows generally do not give accurate results when extended to three-dimensional turbulent flows. It appears that even the most refined Reynolds-stress models do not adequately predict the cross-stream turbulent intensities and the secondary shear stresses that are important for the streamwise vorticity transport.

Liandrat, Aupoix & Cousteix (1987) performed numerical studies with a variety of Reynolds-stress models. They found that simple models based on the Boussinesq (eddy-viscosity) hypothesis provide satisfactory estimates of the mean features of the flow in the case of a single vortex, but fail for a vortex pair. Second-moment closure models improved the prediction of the anisotropy of the normal Reynolds stresses $\langle v'^2 - w'^2 \rangle$, and the development of the secondary flow and streamwise vorticity was computed more accurately than with eddy-viscosity models. Although the prediction of the secondary shear stresses was improved, they were still underestimated. Sankaran & Russell (1990) and Kim & Patel (1994) carried out numerical studies of common-flow-down vortex pairs using $K - \epsilon$ models. In general, the flow in regions away from the vortex core was predicted well, but the details of the flow in the vortex core were captured poorly. The peak streamwise vorticity decayed excessively fast in the streamwise direction.

Large-eddy simulation (LES) is an intermediate method between direct numerical simulation (DNS) and the solution of the Reynolds-averaged Navier–Stokes equations (RANS). In DNS all the turbulent scales are resolved, but its cost limits this technique to low-Reynolds-number turbulent flows. In LES, the computational grid is sufficiently fine to resolve the dynamically important motions, but not the small-scale motions, which are modelled. Therefore, the computational resources required are significantly less than for DNS, and LES can compute flows at higher Reynolds numbers. Since the small-scale motions tend to be more universal, the modelling in LES can be significantly simplified, compared with RANS, and the results can be more accurate than those obtained by current Reynolds-stress models, especially in flows such as this one where non-gradient effects are significant. To improve the understanding of the mechanisms controlling the Reynolds stresses and the current RANS modelling techniques, an analysis of the Reynolds-stress transport equations is needed, and, although the detailed measurements of the mean-flow and turbulence quantities made in experiments have improved the understanding of the three-dimensional characteristics of these types of flows, the data provided by those experiments are still not sufficient for a complete transport-equation analysis. LES is expected to predict with sufficient accuracy turbulence statistics of physical and engineering interest, and to serve as a tool to improve Reynolds-stress models.

Esmaili (1992) and Esmaili & Piomelli (1992) performed LES of a common-flow-down vortex pair embedded in a temporally developing zero-pressure gradient turbulent boundary layer and in a sink-flow boundary layer. Although their results were averaged over a sample of insufficient size, the main features of the Reynolds stresses were captured.

In the present paper common-flow-down vortices are studied, again using LES, but this time in a spatially developing boundary layer. Such a simulation is more realistic,

and can provide better statistically averaged results than the temporally developing simulations performed so far. Sections 2 and 3 will describe the numerical methods used in the simulation, and the geometric configuration, §§4 and 5 will present the mean flow and Reynolds stresses, and §6 will discuss the second-moment budgets. Conclusions will be drawn in §7.

2. Numerical method

In large-eddy simulations the flow variables are decomposed into a large-scale (or resolved) component, denoted by an overbar, and a subgrid-scale component. The large-scale component is defined by the filtering operation:

$$\overline{f}(\boldsymbol{x}) = \int_D f(\boldsymbol{x}')G(\boldsymbol{x},\boldsymbol{x}')\mathrm{d}\boldsymbol{x}', \tag{2.1}$$

where D is the entire computational domain, and G is the filter function.

Applying the filtering operation to the incompressible Navier–Stokes equations yields

$$\frac{\partial \overline{u}_i}{\partial t} + \frac{\partial}{\partial x_j}\left(\overline{u}_i\overline{u}_j\right) = -\frac{\partial \overline{p}}{\partial x_i} - \frac{\partial \tau_{ij}}{\partial x_j} + \frac{1}{Re_{\delta^*}}\frac{\partial^2 \overline{u}_i}{\partial x_j \partial x_j}, \tag{2.2}$$

$$\frac{\partial \overline{u}_i}{\partial x_i} = 0, \tag{2.3}$$

where reference-length (the inflow displacement thickness, δ^*) and velocity (the free-stream velocity, U_∞) scales are used to make $\overline{u}_i$, $\overline{p}$, x_i and t dimensionless. The subgrid-scale stresses, $\tau_{ij} = \overline{u_i u_j} - \overline{u}_i\overline{u}_j$, need to be modelled to represent the effect of the subgrid scales on the resolved field.

Since the small scales tend to be more universal than the large scales, their effects can be modelled by fairly simple eddy-viscosity models of the form

$$\tau_{ij} - \tfrac{1}{3}\delta_{ij}\tau_{kk} = -2\nu_T\overline{S}_{ij} = -2C\overline{\Delta}^2|\overline{S}|\overline{S}_{ij} = -2C\beta_{ij} \tag{2.4}$$

where δ_{ij} is Kronecker's delta, and $|\overline{S}| = (2\overline{S}_{ij}\overline{S}_{ij})^{1/2}$ is the magnitude of the large-scale strain-rate tensor $\overline{S}_{ij} = \left(\partial\overline{u}_i/\partial x_j + \partial\overline{u}_j/\partial x_i\right)/2$. In the present work the model coefficient C is calculated by a localized version (Liu 1994) of the dynamic eddy-viscosity model (Germano *et al.* 1991). In the dynamic eddy-viscosity model, a second filter, the test filter $\widehat{G}$, is introduced, and the coefficient C is computed using an identity relating the resolved turbulent stresses $\mathscr{L}_{ij} = \widehat{\overline{u}_i\overline{u}_j} - \widehat{\overline{u}}_i\widehat{\overline{u}}_j$, the subgrid-stresses τ_{ij} and the subtest-scale stresses $T_{ij} = \widehat{\overline{u}_i\overline{u}_j} - \widehat{\overline{u}}_i\widehat{\overline{u}}_j$ (Germano 1992):

$$\mathscr{L}_{ij} = T_{ij} - \widehat{\tau}_{ij}. \tag{2.5}$$

If the subtest-scale stresses are parameterized by a model of the form (2.4):

$$T_{ij} - \delta_{ij}T_{kk}/3 = -2C\widehat{\overline{\Delta}}^2|\widehat{\overline{S}}|\widehat{\overline{S}}_{ij} = -2C\alpha_{ij}, \tag{2.6}$$

Equations (2.4) and (2.6) can be substituted into (2.5) to yield

$$\mathscr{L}_{ij} - \delta_{ij}\mathscr{L}_{kk}/3 = -2C\alpha_{ij} + 2\widehat{C\beta_{ij}}. \tag{2.7}$$

The calculation of C from (2.7) may result in a mathematical inconsistency if C is extracted from the filtering operation (Cabot & Moin 1993); to avoid the inconsistency, Ghosal *et al.* (1995) used a variational formulation, in which an integral equation was solved iteratively, at a significant additional expense. In the present

simulation, instead, an approximate localization is used in which the identity (2.5) is rewritten as

$$\mathscr{L}_{ij} + \widehat{\tau_{ij}} - \tau_{ij} = T_{ij} - \tau_{ij}. \tag{2.8}$$

Substituting (2.4) and (2.6) into the right-hand side of (2.8) gives

$$\mathscr{L}_{ij} + \widehat{\tau_{ij}} - \tau_{ij} - \delta_{ij}(\mathscr{L}_{kk} + \widehat{\tau_{kk}} - \tau_{kk})/3 = -2C\left(\beta_{ij} - \alpha_{ij}\right). \tag{2.9}$$

At each timestep, the model coefficient can then be evaluated from (2.9), which is a set of algebraic equations for C, using the least-squares approach (Lilly 1992), in a consistent manner:

$$C = -\frac{1}{2}\frac{\left(\mathscr{L}_{ij} + \widehat{\tau_{ij}} - \tau_{ij}\right) M_{ij}}{M_{ij}M_{ij}} \tag{2.10}$$

where $M_{ij} = \alpha_{ij} - \beta_{ij}$.

The terms in (2.10) are obtained from the velocity fields at the timestep n, except for the eddy viscosity, which must be evaluated at the previous timestep; the subgrid-scale stress in the numerator is $\tau_{ij} = -2\nu_T^{n-1}\overline{S}_{ij}^{n}$. It is only approximate in the sense that it assumes C to be a slowly varying function of time; this, however, is a more realistic assumption than the one that requires it to be a slowly varying function of space. *A priori* tests by Lund, Ghosal & Moin (1993), for instance, indicate that in homogeneous turbulence the coefficient is highly correlated in time. To avoid the numerical instabilities that may arise from such temporal correlation, the eddy viscosity is required to be smooth on the test-cell level (i.e. is filtered over the test cell), and the total viscosity is required to be non-negative. This model was tested for the LES of a two-dimensional turbulent boundary layer flow, and the results were in good agreement with DNS and experimental data (Liu 1994).

To avoid the difficulties associated with the implementation of inflow/outflow boundary conditions, the fringe method (Spalart & Watmuff 1993) is employed. This method divides the flow domain into three regions: two fringe regions and a useful region (figure 1*a*). In the fringe regions, extra terms are introduced into the governing equations to remove mass from the boundary layer, reducing the boundary-layer thickness as the flow enters or re-enters the useful region, so that periodic boundary conditions can be implemented in the streamwise direction. In the useful region, the governing equations are the Navier–Stokes equations; only the results in this area are of interest. The streamwise vortices are introduced by a body force (which acts as a numerical vortex generator) placed before the useful region of the boundary layer. The momentum equations, with fringe terms and body force included, are of the form

$$\frac{\partial \overline{u}_i}{\partial t} + \frac{\partial}{\partial x_j}\left(\overline{u}_i\overline{u}_j\right) = -\frac{\partial \overline{p}}{\partial x_i} - \frac{\partial \tau_{ij}}{\partial x_j} + \frac{1}{Re_\delta}\frac{\partial^2 \overline{u}_i}{\partial x_j \partial x_j} - u_{2,j}\frac{\partial \overline{u}_i}{\partial x_j} + F_i, \tag{2.11}$$

where $u_{2,j}$ is the fringe velocity and F_i the body force.

The fringe velocity, $u_{2,j}$, is given by (Spalart & Watmuff 1993)

$$u_{2,1} = u_{2,3} = 0, \qquad u_{2,2} = -S\frac{y^2}{y + y_1}\left[\mathrm{e}^{-x^2/x_1^2} + \mathrm{e}^{-(L_x - x)^2/x_1^2}\right], \tag{2.12}$$

where S is the strength of the fringe terms, L_x is the computational domain size in the streamwise direction, and x_1 determines the width of the fringe region. The parameter y_1 and the strength S control the boundary-layer thickness at the inflow of the useful region.

Many experiments show that the velocity distribution of the embedded vortices is

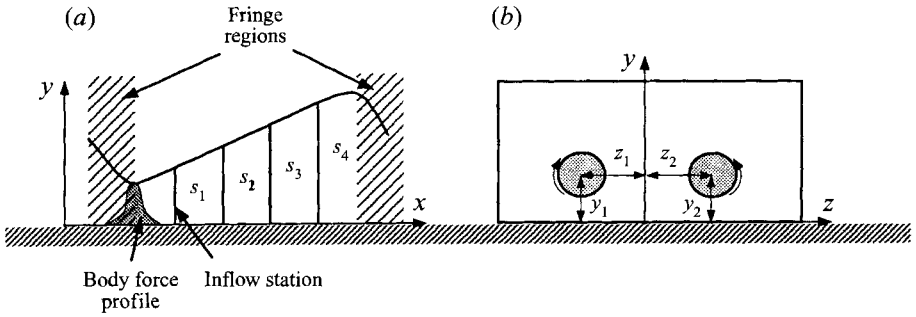

FIGURE 1. Flow configuration and the computational domain. (*a*) (x, y)-plane; (*b*) (y, z)-plane.

very similar to that of Oseen vortices (plus their images to account for the effect of the solid wall). If the velocity profile in the region of non-zero body force F_i (as shown in figure 1) is $v_\theta \sim (v_{2d})_\theta f(x)$, where $(v_{2d})_\theta$ is the cross-plane velocity of the vortex and $f(x)$ is the streamwise variation of the vortex strength, the steady-state θ-momentum equation in this region can be approximated as

$$U_\infty (v_{2d})_\theta \frac{\mathrm{d}f}{\mathrm{d}x} \sim F_\theta. \tag{2.13}$$

Introducing the Oseen vortex velocity profile $(v_{2d})_\theta = \left[1 - \exp\left(-r^2/\sigma^2\right)\right] \Gamma/2\pi r$ (where Γ is the circulation, r is the distance from the axis of the vortex, and σ is the core size) into the above equation yields a body force of the form

$$F_\theta = S_v \frac{1 - \mathrm{e}^{-r^2/\sigma^2}}{r/\sigma} g(x), \tag{2.14}$$

where S_v is the strength, and $g(x)$ controls the streamwise variation of the body force; it was chosen to be of the form $g(x) = \mathrm{e}^{-(x-x_v)^2/x_2^2}$ (that is, $f(x)$ is an error function). The parameters x_v and x_2 denote the streamwise location and spatial extent of the body force. In addition, to account for the effect of the solid wall, the images of the distribution (2.14) are also added in the present simulations, and the body force is modified in the region close to the wall to satisfy the no-slip boundary condition.

Since a momentum deficit is introduced by actual vortex generators (e.g. delta wings) in the experiments, this effect is included. A Gaussian distribution is again used in the streamwise direction; the streamwise component F_1 of the body force, therefore, is

$$F_1 = S_w \, \mathrm{e}^{-\ln 2(r/\sigma)^2} g(x), \tag{2.15}$$

where S_w determines the strength of the wake. The constant $\ln 2$ is used to let the magnitude of F_1 at the core edge be half the maximum magnitude. A simulation was also performed in which the wake profile was not introduced (Liu 1994). A slight axial acceleration was observed near the vortex centre, due to the low pressure in the core, that is not realistic.

The governing equations (2.2) and (2.3) are integrated in time using a Fourier–Chebychev pseudospectral collocation scheme (Zang & Hussaini 1988). The skew-symmetric form of the momentum equation (2.2) is employed, and the time-advancement is performed by a fractional-timestep method with a semi-implicit scheme; the wall-normal diffusion term is advanced using the Crank–Nicolson scheme, and

the remaining terms by a low-storage third-order Runge–Kutta scheme. Periodic boundary conditions are applied in the streamwise (x) and spanwise (z) directions, and no-slip conditions at the solid wall; asymptotic boundary conditions are applied at the upper boundary. No dealiasing is performed.

3. Geometric configuration

Since the common-flow-down vortices decay slowly in the streamwise direction, the computational domain must be fairly long to include a significant development of these vortices; since they move apart in the spanwise direction, a large spanwise width is also required. The domain size used here is $600\delta^* \times 40\delta^* \times 100\delta^*$ in the streamwise, wall-normal and spanwise directions respectively. Unless otherwise stated, δ^* is the displacement thickness at the inflow location in the undisturbed boundary layer, located at $0.2L_x$ (L_x is the streamwise length of the domain). In the undisturbed boundary layer, $Re_{\delta^*} = 830$ at the inlet, and $Re_{\delta^*} = 1660$ at the ouflow. The number of grid points in the three directions is $192 \times 73 \times 128$. The grid size is $\Delta x = 3.1\delta^*$ and $\Delta z = 0.78\delta^*$ in the streamwise and spanwise directions, or, in wall units at the inflow, $\Delta x^+ = 125$ and $\Delta z^+ = 31$; the distance of the first point from the wall is approximately $y^+ = 0.2$. The necessity of a fairly large computational box and the grid resolution required by the LES limit the Reynolds number of this calculation. The maximum grid spacing allowable in the spanwise direction when the wall layer is resolved is $\Delta z^+ \simeq 45$. In the present calculation, because of the convection effects of the embedded vortices, the wall shear is increased immediately below and inboard of the vortices; this resuts in a higher value of the local friction velocity. The resolution was chosen in such a way that the maximum grid spacing, in wall units, is $\Delta z^+_{max} = 40$ below the vortex. Increasing the Reynolds number to match the experiment would have required a significantly finer grid, and the calculation would have been prohibitively expensive.

Most of the data reported were obtained at the four cross-planes located at $x/L_x \simeq 0.2$, 0.4, 0.6, and 0.8, shown in figure 1(*a*). They correspond to $x/\delta^* = 122$, 244, 366, and 488. At the inflow location, $x/\delta^* = 122$, the coordinates of the vortex centres, shown in figure 1(*b*), are $z_1/\delta^* = -z_2/\delta^* = 11$, $y_1/\delta^* = y_2/\delta^* = 5$, and the size of each vortex core is $\sigma/\delta^* = 2.1$.

The strength of the body force is $S_v = 0.026U_\infty^2/\delta^*$, obtained by matching the vorticity at the inflow station to the experimental data of Pauley & Eaton (1988*a*, *b*). The inflow vorticity is $\Omega_x = 0.32U_\infty/\delta^*$, the maximum magnitude of the secondary flow is $V_\theta = 0.28U_\infty$, and the inflow vortex Reynolds number is $\Gamma/\nu = 5000$. The strength of the wake component of the body force, F_1, is $S_w = 0.028U_\infty^2/\delta^*$. To eliminate the returning vortices, introduced by the streamwise periodic boundary conditions, a body force with the same configuration as (2.14), and opposite sign, is placed some distance downstream of the outflow boundary.

4. Mean-flow development

The solution fields were averaged over a time interval of $600\delta^*/U_\infty$, and also using symmetry about the plane $z = 0$ (however, many figures show both sides for clarity). In the following, $\langle\cdot\rangle$ will represent statistics obtained using the entire sample. A prime will denote the large-scale fluctuation (e.g. $u' = \bar{u} - \langle\bar{u}\rangle$) and a capital letter a time-averaged quantity (e.g. $U = \langle\bar{u}\rangle$). To evaluate the adequacy of the sample size, two sets of statistics averaged over samples of different sizes were compared. If $\langle\cdot\rangle_h$ represents

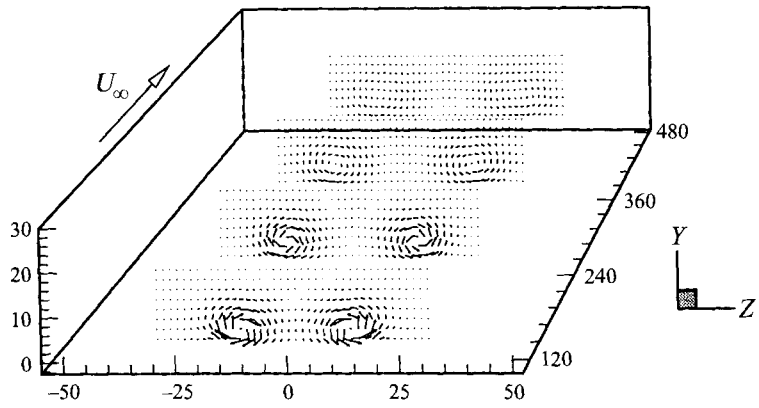

FIGURE 2. Secondary velocity vectors at the four streamwise stations.

statistics averaged over $300\delta^*/U_\infty$, the difference between the full and the reduced sets are $\|U - U_h\|/U_\infty < 0.01\%$ and $\|\langle u'v'\rangle - \langle u'v'\rangle_h\|/|\langle u'v'\rangle_{max}| < 0.5\%$ when averaged over a cross-plane; worst-case local differences for U and $\langle u'v'\rangle$ are less than 0.6% and 4%, respectively. As mentioned before, the vortex strength is adjusted to match the experimental data of Pauley & Eaton (1988*a*) at their $X = 66$ cm station; the LES results at the second station will be compared with the corresponding location in the experiment, namely the $X = 97$ cm station. The major difference is that the Reynolds number in the calculation is only one third of that in the experiment.

Figure 2 shows the secondary velocity vector fields at the four streamwise stations. The vortices move apart due to the image vortices, and turbulent diffusion makes them grow in size and decay in vorticity. Nevertheless, the peak streamwise vorticity decreases from about 0.3 to about 0.05, compared with the undisturbed spanwise vorticity which is about 0.05. This led us to describe the vortices as strong.

As mentioned in §2, the goal of the body force is to generate Oseen vortices. The vortex velocity profiles at the inflow station are compared with those of a common-flow-down Oseen vortex pair in Figure 3(*a*, *b*); the profiles generated by the body force are quite close to those of the Oseen vortex. Perfect agreement is not expected because U_∞ in (2.13) is only an approximation.

The V and W velocity compare quite well with the experimental data of Pauley & Eaton (1988*a*, *b*) in figure 3(*c*, *d*). However, close to the wall the spanwise velocity is smaller in the calculation. The decay between the first two locations (figures 3*a* and 3*c*) appears excessively rapid. This could result from the Reynolds-number difference, or from the differences that remain between a true vortex generator and its representation by a body force. The positive peak of W is accurate, therefore the difference seems to be confined to the wall region. Note also that in the experiment the streamwise velocity (shown below) is monotonic up to $y/\delta^* \approx 1.5$ ($y^+ \approx 160$), but the spanwise velocity peaks below $y/\delta^* = 0.5$ ($y^+ \approx 50$). Such a difference in limiting behaviour implies surprisingly large turning angles in the buffer layer.

Streamwise-velocity contours shown in figure 4 reveal the considerable distortion of the boundary layer by the vortices, as well as the velocity deficit. Figure 5 compares the streamwise velocity at the second station with experimental data at $X = 97$ cm. The agreement is very good, including the velocity deficit, in spite of the Reynolds-number difference. The large distortion of the flow is again vivid. Relative to the undisturbed flow, the spanwise average of the manipulated flow has lower integral

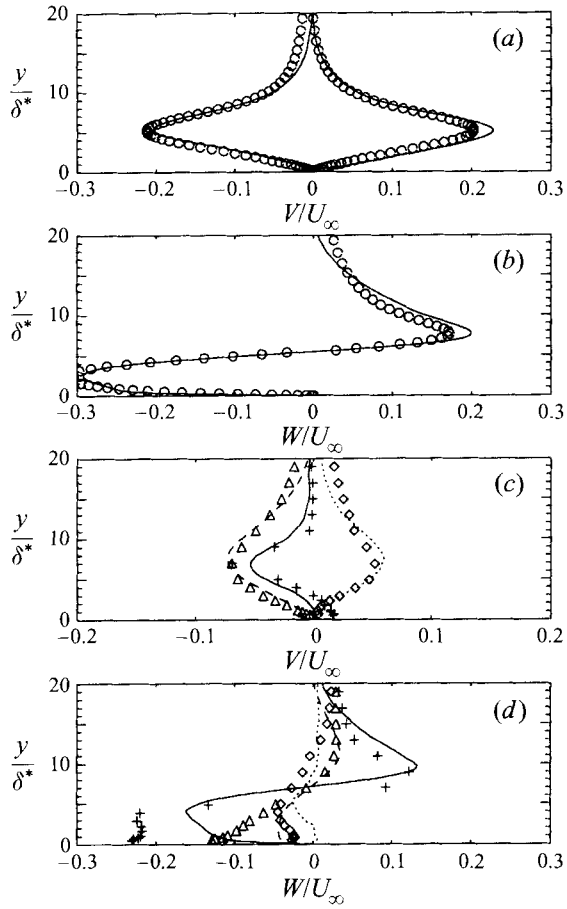

FIGURE 3. Vortex velocity profiles at the first and second locations. (*a*) Wall-normal velocity along the vertical lines at $z/\delta^* = 10$ and $z/\delta^* = 16$ (the edges of the vortex core) at the first location: ———, body force; ○, Oseen vortex. (*b*) Spanwise velocity along the vertical line passing through the vortex centre ($z/\delta^* = 13$) at the first location, lines and symbols as in (*a*). (*c*) Wall-normal velocity at the second location, lines: LES, symbols: experiment. – – –, △, Downwash region ($z/\delta^* = 10$); ———, +, vortex centre ($z/\delta^* = 16$); ·····, ◇, upwash region ($z/\delta^* = 22$). (*d*) Spanwise velocity at the second location, lines and symbols as in (*c*).

thicknesses and a lower shape factor $H \equiv \delta^*/\theta$. These lower values only persist until the vortices collide with their common-flow-up neighbours, and this probably motivates the current preference for co-rotating vortices in applications.

The streamwise velocity profiles expressed in local wall units at several spanwise locations are shown in figure 6. The immediate downwash location ($z/\delta^* = 13$) has the highest, and the immediate upwash location ($z/\delta^* = 19$) has the lowest wall shear stress. The vortex-centre profile and the profile in the immediate downwash region deviate the most from the undisturbed profile, and present some characteristics of laminar profiles: in particular, they are higher than the standard logarithmic layer. The deviations are larger than those found by Pauley & Eaton (1988*a*, *b*), probably due to the difference in Reynolds numbers. The undisturbed Reynolds number in the simulation is close to the critical Reynolds number for the existence of a normal

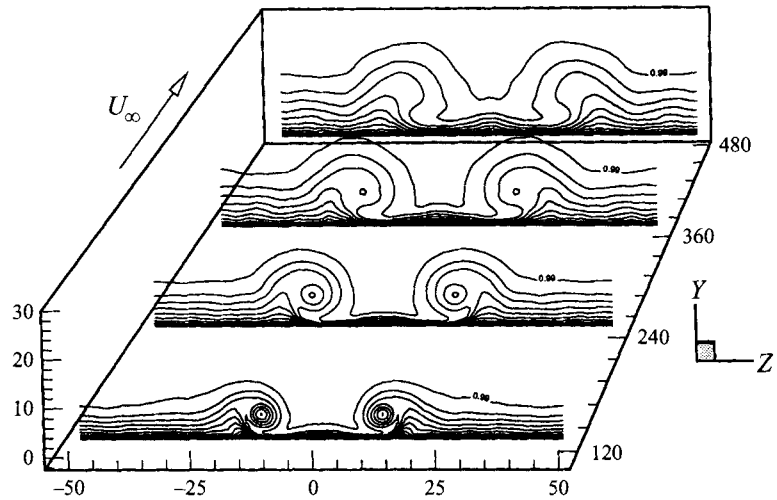

FIGURE 4. Streamwise velocity contours at the four streamwise stations.

log layer (Spalart 1988); in the thin region of the boundary layer the local Reynolds number is lower than the critical value, leading to a partial relaminarization.

Streamwise-vorticity contours are shown in figure 7. The primary vorticity diffuses outward from the vortex centre, and decays in the streamwise direction. A layer of secondary vorticity with opposite sign exists close to the wall due to the no-slip boundary condition; this layer can be seen more clearly in figure 8, at the second station. In the downwash region and underneath the vortex, the secondary vorticity is confined to a very thin layer and its maximum value, which occurs at the wall, is larger than that of the embedded one. The secondary streamwise vorticity corresponds to the spanwise skin friction. In the upwash region, on the other hand, the secondary vorticity is convected towards the outer layer with much weaker strength; a clear rolling-up of a secondary vortex, as observed in laminar flows (Esmaili 1992), does not occur.

The streamwise development of the primary peak vorticity and of the circulation of the quarter-plane $z > 0$ are shown in figure 9. In order to compare with the experimental data, the circulation is calculated by the same technique as in Pauley & Eaton (1988*a*, *b*): only the vorticity with the same sign as the embedded vorticity is used in the integration. The vorticity decays slightly faster than in the experimental data, possibly due to the lower Reynolds number. The $K-\epsilon$ model simulation shows an excessive decay of the peak vorticity; this is also observed in free vortices and motivates much turbulence-modelling work, from algebraic to full-Reynolds-stress models. The argument that rotation damages the correlation between the Reynolds-stress and the strain tensors (essentially, the turbulence production) seems widely accepted. The circulation decays more slowly than the peak vorticity, and the three predictions of the circulation agree very well with each other. Diffusion affects the circulation much less than the peak vorticity.

5. Second moments

In this section, the large-scale Reynolds stresses, $R_{ij} = \langle u_i' u_j' \rangle$ are presented; the mechanisms that control their behaviour will be discussed in the next section. Since the

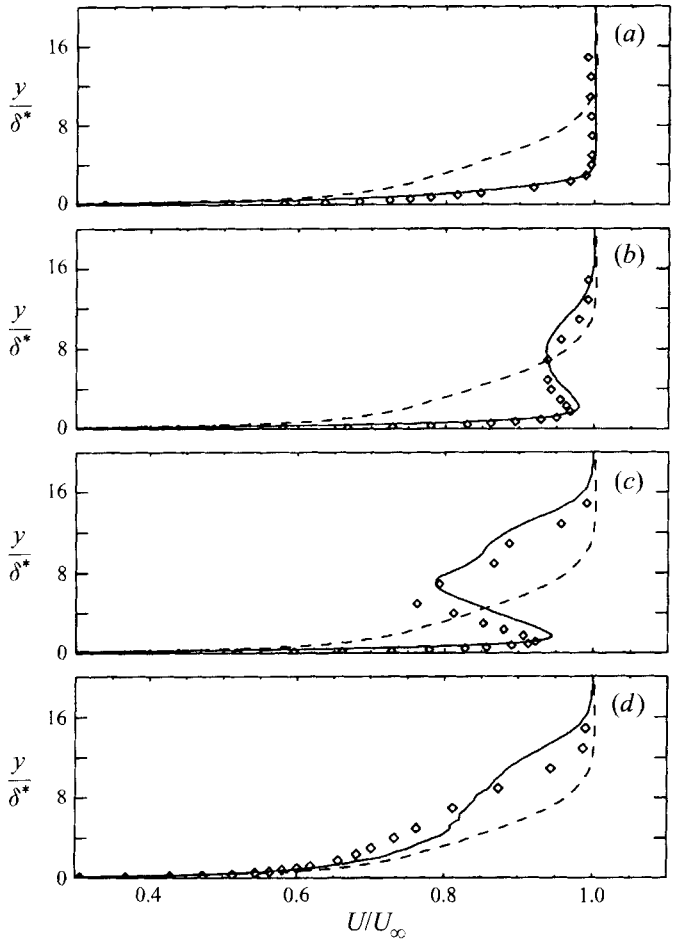

FIGURE 5. Streamwise velocity profiles at the second streamwise station compared with the experimental data of Pauley & Eaton (1988*a*,*b*) at $X = 97$ cm. ———, LES; – – –, undisturbed boundary layer; ◇, experiment; (*a*) between vortices ($z/\delta^* = 0$), (*b*) downwash region ($z/\delta^* = 10$), (*c*) vortex centre ($z/\delta^* = 16$), (*d*) upwash region ($z/\delta^* = 22$).

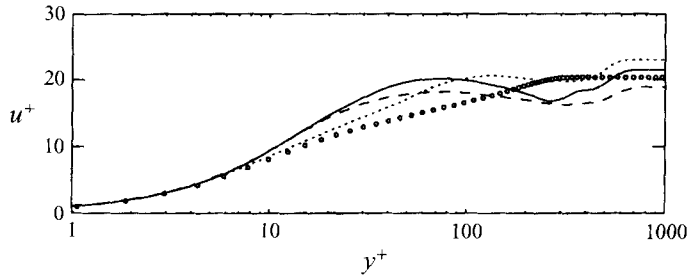

FIGURE 6. Streamwise velocity profiles in local wall units at the second streamwise station. ○, Undisturbed boundary layer; – – –, immediate downwash region ($z/\delta^* = 13$); ———, vortex center ($z/\delta^* = 16$); ·····, immediate upwash region ($z/\delta^* = 19$).

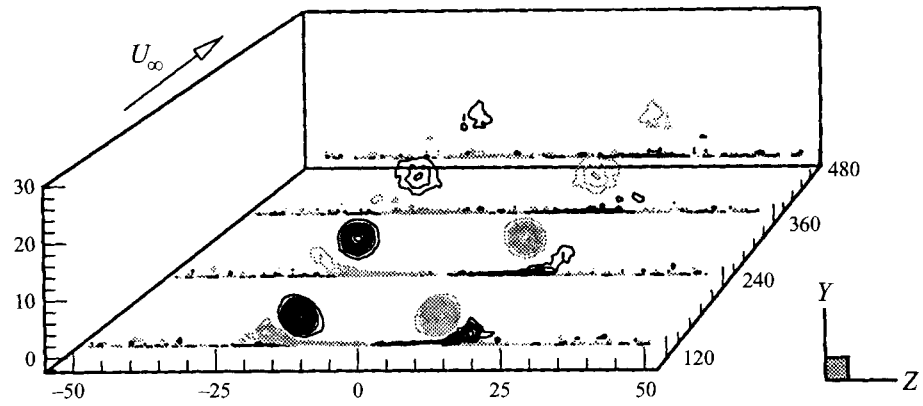

FIGURE 7. Contours of streamwise vorticity at the four streamwise stations. Grey: negative contours, black: positive contours.

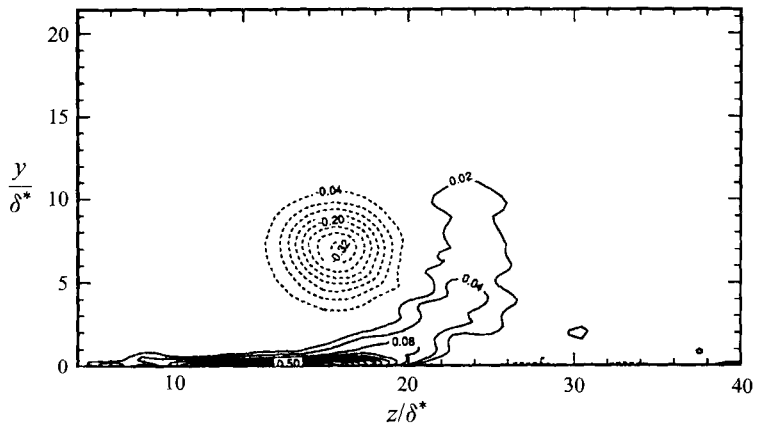

FIGURE 8. Contours of streamwise vorticity at the second streamwise station.

subgrid-scale stresses are an order of magnitude smaller than the large-scale stresses in the present simulation (at least away from the walls), the large-scale quantities shown in the following represent the contributions from most of the significant turbulent motions.

Figure 10 shows the large-scale turbulent kinetic energy $q^2 = \langle u_i' u_i' \rangle$ at the second station. Simulation and experiment agree rather well, suggesting a satisfactory recovery from the large difference between the two vortex generators (the shift in spanwise position could be due to the induced velocity of the vortex bound to the vortex generator, which is absent in the simulation). However, the simulation results are consistently higher, even in the undisturbed region.

Similar to the streamwise vorticity, the turbulent kinetic energy is confined to a thin layer in the downwash region, and lifted up in the upwash region. The magnitude of q^2 in this 'tongue' is approximately 50% higher than in the experimental data, partly due to the difference of the Reynolds numbers (higher skin-friction coefficient at lower Reynolds number). The factor of 3 in the Reynolds number can explain about half of the 50% difference. High levels of turbulent kinetic energy are also found in the vortex core, with magnitude around 40% higher than that in the experiment.

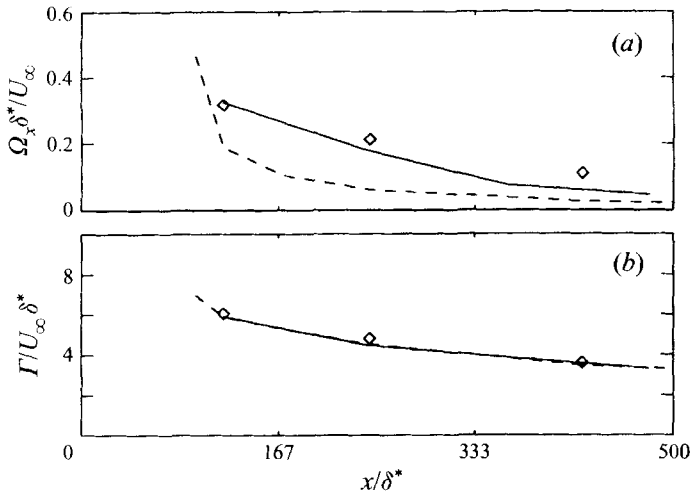

FIGURE 9. (*a*) Streamwise vorticity at vortex centres, (*b*) circulation of the half-cross-planes ($z > 0$). ———, Present simulation; – – –, $K-\epsilon$ model simulation of Kim & Patel (1994), ◇, experiment of Pauley & Eaton (1988*a*, *b*).

The mechanism responsible for these high levels of turbulent kinetic energy will be discussed in the next section.

The profiles of the large-scale turbulence intensities, u'_{rms}, v'_{rms} and w'_{rms}, normalized in local wall units, are shown in figure 11. Near the wall, the downwash region shows a distinct suppression of the turbulence, but it is far from complete relaminarization. The streamwise intensity is less affected than the other components, much like in a two-dimensional turbulent boundary layer with wall suction (Antonia, Spalart & Mariani 1994). Closer to the vortex the profiles have peaks in the outer layer as expected from figure 10; the peak u'_{rms} is relatively lower than the others. This suggests that production through $\partial U/\partial y$ associated with the axial deficit is modest (recall that that production directly 'feeds' u'_{rms}, which feeds the other components through the pressure term). The 'lifted' kinetic energy is also seen.

The combinations of Reynolds stresses $\langle w'^2\rangle - \langle v'^2\rangle$ and $\langle v'w'\rangle$ control the vortex decay. Figure 12 shows the former quantity at the second station, compared with the experimental data. The patterns are very similar, and consistent both with the four-way symmetry of an axisymmetric vortex and with lifting of turbulence from the wall. However, the simulation results are again higher. Similar remarks apply to the latter quantity (not shown). Grid-refinement studies indicate that the magnitude difference between the simulation and the experiment is not caused by the grid resolution. Besides the Reynolds-number effect, the uncertainty in the experimental measurement can be significant. Bradshaw (1987) mentioned that the cross-plane shear stress $\langle v'w'\rangle$ is particularly difficult to measure: its uncertainty is the largest one in measurements of the second moments; the estimated uncertainty for $\langle v'w'\rangle$ in X-wire measurements was 15% of $\langle u'v'\rangle$, with an additional error of 9% of $\langle u'v'\rangle$ when the probe was not aligned with the mean flow (Anderson & Eaton 1987; Pauley & Eaton 1988*a*). Since the region of significant $\langle v'w'\rangle$ is concentrated in small areas in this case, the uncertainty of the maximum $\langle v'w'\rangle$ can be even larger.

Figure 13 shows the primary large-scale Reynolds shear stress $-\langle u'v'\rangle$ at the second streamwise station, compared with the experimental data. In the upwash region,

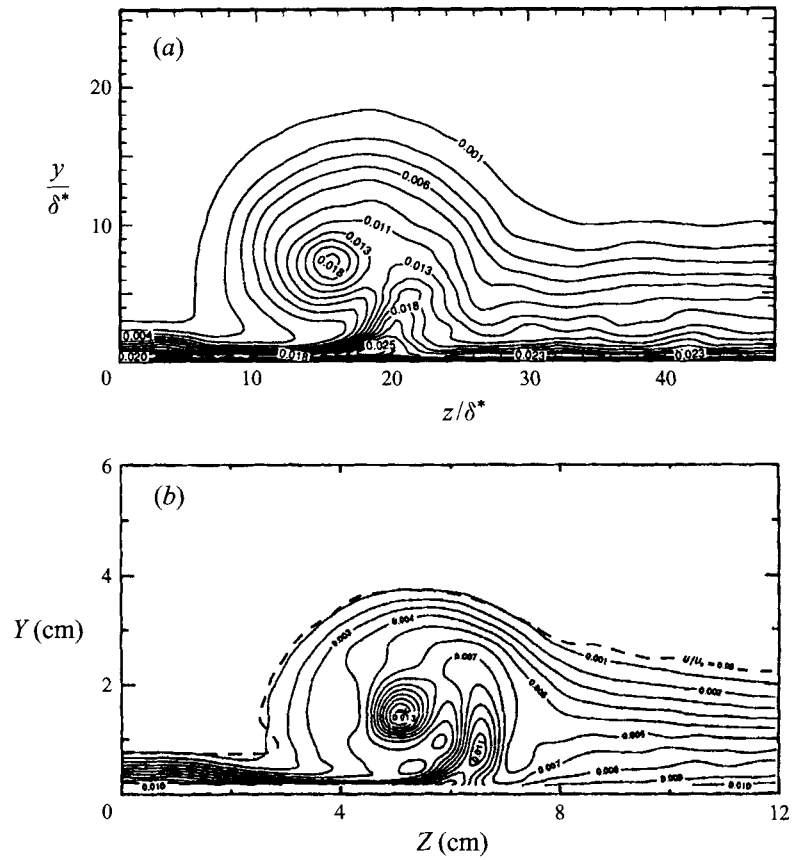

FIGURE 10. Contours of turbulent kinetic energy, q^2/U_∞^2: (*a*) second streamwise station, (*b*) experimental data of Pauley & Eaton (1988*a*) at $X = 97$ cm. The reference δ^* in the experiment was 0.25 cm.

the embedded vortices convect high levels of $-\langle u'v' \rangle$ from the wall layer into the outer layer, producing a region of positive $-\langle u'v' \rangle$ rolling around and above the vortex core. The peak above the vortex core in the simulation is again 50% higher than in the experiment. The maximum value also occurs in the immediate upwash region close to the wall, similar to that of the turbulent kinetic energy. In the vortex core the distribution presents a more complicated pattern, with a region of negative $-\langle u'v' \rangle$, and a small region with high levels of positive $-\langle u'v' \rangle$ on the downwash side of the vortex centre. High levels of negative $-\langle u'v' \rangle$ are concentrated in a small area on the upwash side of the centre. In a simulation that did not include the wake-deficit profile (Liu 1994), only a negative region roughly centred on the vortex centre was observed in the vortex core, which indicates that the velocity deficit has an important effect on the distribution of $-\langle u'v' \rangle$. While the peak value on the downwash side of the vortex centre matches very well the experimental data, on the upwash side the peak is 20% larger. The agreement is better than for other moments. It will be shown later that the transport from the immediate upwash region has less effect on the shear stress $-\langle u'v' \rangle$ in the vortex core than on turbulent kinetic energy, and that $-\langle u'v' \rangle$ in the vortex core is mainly due to the velocity deficit.

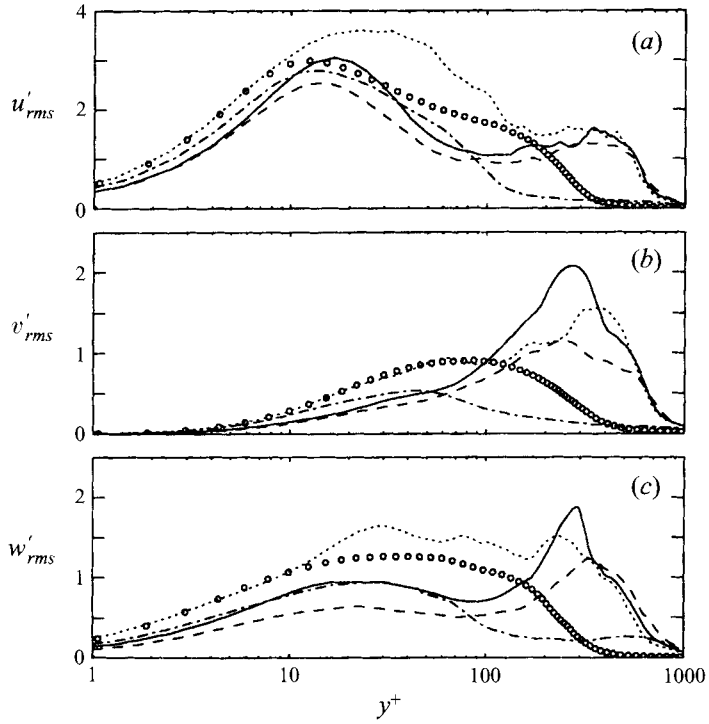

FIGURE 11. Large-scale turbulent intensities normalized by the local friction velocity at the second streamwise station. (*a*) Streamwise, (*b*) vertical, (*c*) spanwise. ○, Undisturbed boundary layer; — · — ·, between vortices ($z/\delta^* = 0$); – – –, immediate downwash region ($z/\delta^* = 13$); ———, vortex centre ($z/\delta^* = 16$); ·····, immediate upwash region ($z/\delta^* = 19$).

The secondary Reynolds shear stress $-\langle u'w' \rangle$ (figure 14) is larger than $-\langle u'v' \rangle$ in magnitude in some regions in the flow. Significant negative values of $-\langle u'w' \rangle$ are found in the shape of a tongue similar to the turbulent kinetic energy shown in figure 10; large values also occur close to the wall. Its maximum value is over twice the peak $-\langle u'v' \rangle$, and occurs at the same location as $-\langle u'v' \rangle$ and q^2. The DNS of Sendstad & Moin (1992) showed that, when a two-dimensional boundary-layer flow experiences an extra gradient $\partial W/\partial y$, the magnitude of $\langle u'w' \rangle$ increases dramatically; the DNS of a three-dimensional turbulent boundary layer in which the free-stream vector changes direction at a constant angular velocity also shows a very large magnitude of $\langle u'w' \rangle$, which was found to be Reynolds-number dependent (Spalart 1989). In both of these flows, the associated strain rate $\partial U/\partial z + \partial W/\partial x$ was zero, so that there was no energy exchange with the mean flow. Here, the lifting of low-speed fluid creates a local $\partial U/\partial z$ gradient, but direct lifting of the turbulence seems more significant than production (production by $\partial U/\partial z$ would produce two opposite layers in $\langle u'w' \rangle$). Quadrant analysis (Liu 1994) indicates that events with $u' > 0$ and $w' > 0$ are responsible for the region of negative $-\langle u'w' \rangle$ in the immediate upwash region close to the wall. Near the vortex core, $\langle u'w' \rangle$ has the same two-way symmetry as $\langle u'v' \rangle$, as opposed to the four-way symmetry of $\langle v'w' \rangle$. This pattern was not found in the simulation without wake deficit (Liu 1994).

The next section will assist in the improvement of Reynolds-stress turbulence models. For the rest of this section, we turn our attention to Reynolds-averaged (as opposed to subgrid-scale) eddy viscosities, in order to suggest directions for

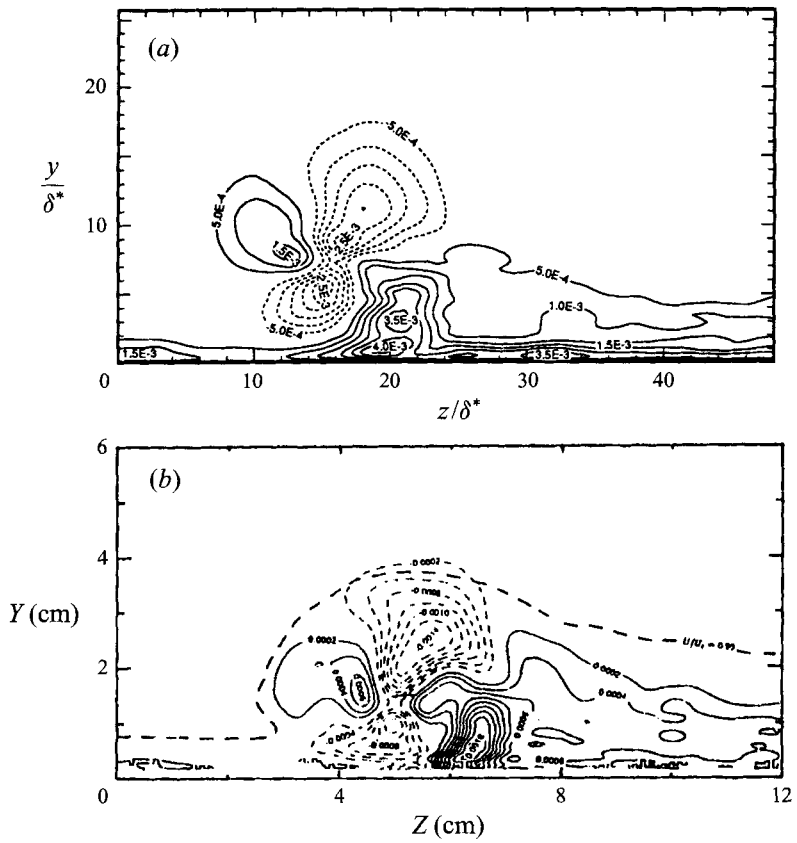

FIGURE 12. Contours of the anisotropy of the normal Reynolds stresses, $-\left(\langle v'^2\rangle - \langle w'^2\rangle\right)/U_\infty^2$: (*a*) second streamwise station, (*b*) experimental data of Pauley & Eaton (1988*a*) at $X = 97$ cm. The reference δ^* in the experiment was 0.25 cm.

improvements of the simple engineering turbulence models. One direction may be a 'non-scalar' eddy viscosity; another, more immediate one, is to bring the magnitude of the modelled eddy viscosity into a plausible range. Both issues are investigated using dot products between the strain and stress tensors, rather than with individual ratios such as $-\langle u'v'\rangle/(\partial U/\partial y)$, to obtain some measure of frame independence.

The anticipated weakness of the (scalar) eddy-viscosity assumption is explored in Figure 15 using the correlation coefficient between the two tensors,

$$\widetilde{R} \equiv \frac{-\langle u_i' u_j'\rangle \langle S_{ij}\rangle}{(\langle u_i' u_j'\rangle \langle u_i' u_j'\rangle)^{1/2} (\langle S_{ij}\rangle \langle S_{ij}\rangle)^{1/2}}; \tag{5.1}$$

the diagonal component of the stress tensor was removed, since it has no influence on the prediction of an incompressible flow. If it were not removed, the numerator of (5.1) would be unchanged, but the denominator would be larger, so that $\widetilde{R}$ would be lower. Deviations of $\widetilde{R}$ from the ideal value of 1 reveal how far the flow deviates from the behaviour a scalar eddy viscosity would impose. Figure 15(*a*) shows few regions above 0.8, and many below 0.2 (but note that the lower bound on $\widetilde{R}$ is -1). The contours are not very smooth, but nevertheless more readable than with individual ratios. In the undisturbed part of the boundary layer, the correlation does not exceed

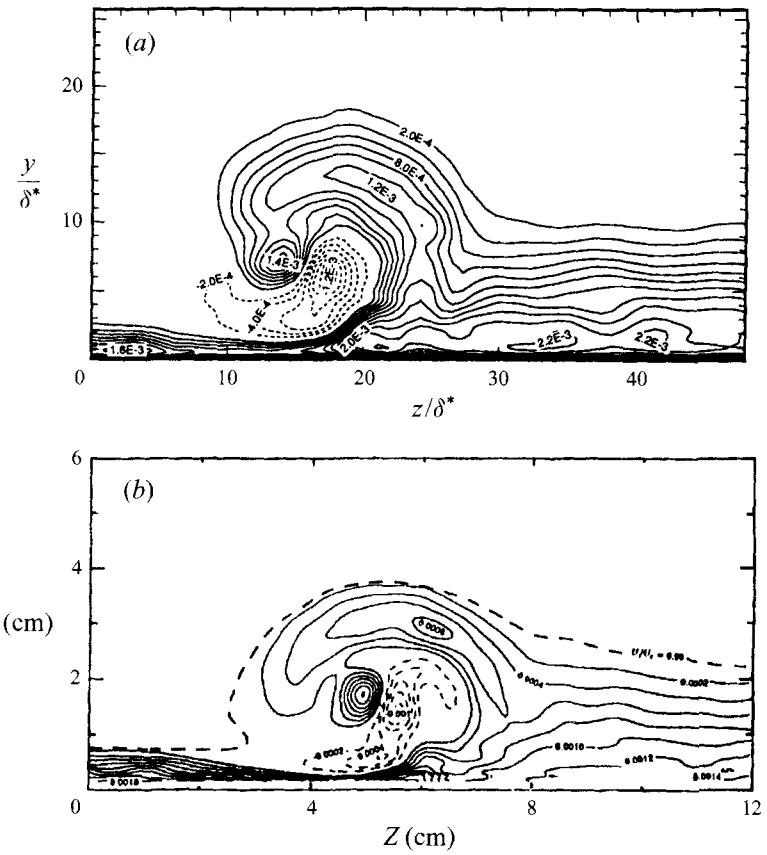

FIGURE 13. Contours of the primary Reynolds stress $-\langle u'v'\rangle/U_\infty^2$: (*a*) second streamwise station, (*b*) experimental data of Pauley & Eaton (1988*a*), $X = 97$ cm. The reference δ^* in the experiment was 0.25 cm.

about 0.7, and is low near the wall. This is, of course, because $\langle u'^2\rangle > \langle v'^2\rangle$ and other inequalities (which have no detrimental effect on the flow field in the two-dimensional boundary layer). Values around 0.7 appear quite tolerable; the troublesome regions are the downwash region, and the vortex core.

In order to determine the specific effect of the eddy-viscosity anisotropy on the vortex decay, $\tilde{R}$ was recalculated in the (y,z)-plane only (that is, i and j were restricted to (2,3) in (5.1)). Away from the vortex, that correlation is very small and has little meaning. Rather high values are found around the vortex, and very low values in the core, where both tensors take small values because of symmetry (and the eddy-viscosity assumption would yield very low Reynolds stresses). This suggests that a free vortex does not in fact catastrophically invalidate the (scalar) eddy-viscosity assumption in itself.

The magnitude of the eddy viscosity is another matter entirely, explored in figure 16. Again a dot product is used to produce an eddy viscosity:

$$\nu_e \equiv -\frac{\langle u_i' u_j'\rangle \langle S_{ij}\rangle}{2\langle S_{ij}\rangle \langle S_{ij}\rangle} \tag{5.2}$$

(the diagonal component of $\langle u_i' u_j'\rangle$ has no effect in this case). The mathematical

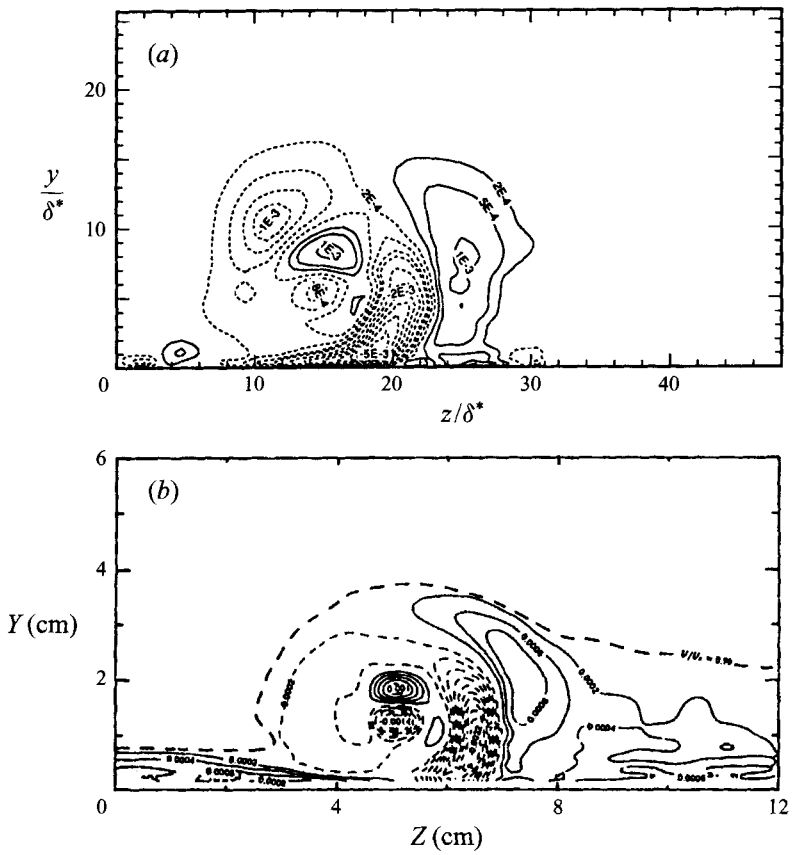

FIGURE 14. Contours of the secondary Reynolds stress $-\langle u'w'\rangle/U_\infty^2$; (*a*) second streamwise station, (*b*) experimental data of Pauley & Eaton (1988*a*) at $X = 97$ cm. The reference δ^* in the experiment was 0.25 cm.

motivation for this 'least-squares' definition is clear; the following physical interpretation can also be put forward: ν_e is the eddy viscosity that would give the correct production rate, transferring the correct amount of kinetic energy from the mean flow to the turbulence. The figure compares this quantity and an eddy viscosity calculated from the $K-\epsilon$ formula, $\nu_e = C_\mu K^2/\epsilon$, with $C_\mu = 0.09$. The LES results for K and ϵ are used instead of an *ab initio* $K-\epsilon$ solution based on the consideration that in an accurate $K-\epsilon$ solution both K and ϵ would be close to the LES values. The values of ν_e predicted by the $K-\epsilon$ formulation are close to those obtained via (5.2) away from the vortex, giving our approach much credibility; inside the vortex, however, they are roughly double the LES values. This explains the rapid decay of vorticity in $K-\epsilon$ solutions (see figure 9), and gives model developers a target range for the desired values in this flow. The quasi-laminar region in the downwash is also evident. We believe the eddy-viscosity magnitude (figure 16) is a more pressing problem than the tensor anisotropy (figure 15), although the latter has received more attention possibly because of its 'qualitative' character.

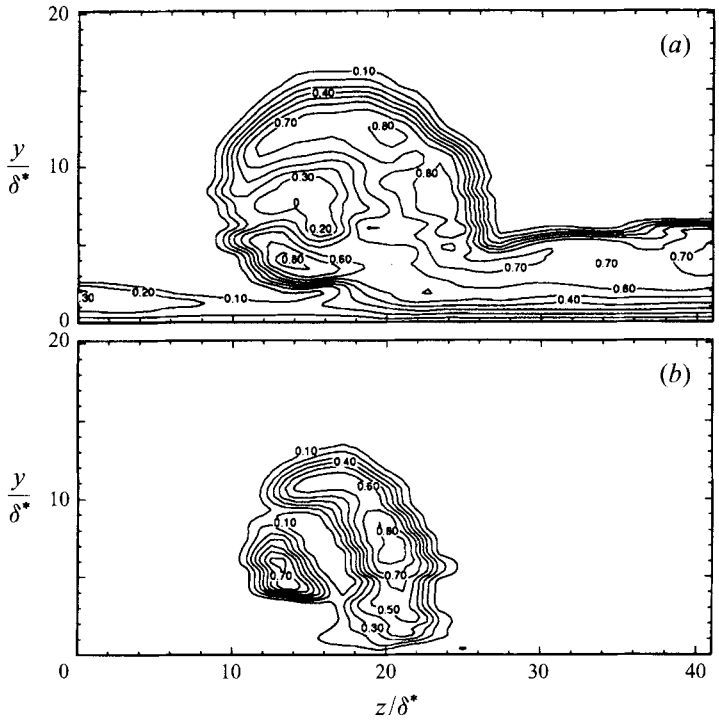

FIGURE 15. Correlation coefficients between strain and stress tensors (see (5.1)) at the second streamwise station. (*a*) Full tensors; (*b*) only components in the (y,z)-plane.

6. Reynolds-stress transport

The transport equation of the large-scale turbulent kinetic energy $K = \langle u_i' u_i' \rangle / 2$ is

$$\frac{\partial K}{\partial t} + U_k \frac{\partial K}{\partial x_k} = \underbrace{-R_{ij} \frac{\partial U_i}{\partial x_j} + \langle \tau_{ij} \rangle \langle \overline{S}_{ij} \rangle}_{\text{production}} - \underbrace{\left(\epsilon - \langle \tau_{ij} \overline{S}_{ij} \rangle\right)}_{\text{dissipation}} + \nu \frac{\partial^2 K}{\partial x_j \partial x_j}$$
$$\underbrace{- \frac{\partial}{\partial x_i} \left\langle \frac{u_k' u_k' u_i'}{2} + p' u_i' + \tau_{ki}' u_k' \right\rangle}_{\text{turbulent diffusion}} \tag{6.1}$$

where the large-scale dissipation rate is $\epsilon = \nu \langle (\partial u_i'/\partial x_j)(\partial u_i'/\partial x_j) \rangle$. The contributions of the subgrid-scale stresses to the production and dissipation are $\langle \tau_{ij} \rangle \langle \overline{S}_{ij} \rangle$ and $\langle \tau_{ij} \overline{S}_{ij} \rangle$. Since the vortices decay slowly in the streamwise direction, the effect of the streamwise gradients of stresses was found to be much weaker than that of the other gradients and is neglected in the following discussion.

The terms retained in the large-scale production of K are

$$-R_{ij} \frac{\partial U_i}{\partial x_j} \simeq -\langle v'^2 \rangle \frac{\partial V}{\partial y} - \langle w'^2 \rangle \frac{\partial W}{\partial z} - \langle u'v' \rangle \frac{\partial U}{\partial y} - \langle v'w' \rangle \left(\frac{\partial V}{\partial z} + \frac{\partial W}{\partial y} \right) - \langle u'w' \rangle \frac{\partial U}{\partial z}. \tag{6.2}$$

The dominant production terms are $-\langle u'v' \rangle \partial U/\partial y$ and $-\langle u'w' \rangle \partial U/\partial z$, shown in figure 17 together with the total production, which includes both large- and small-scale contributions. The first term, $-\langle u'v' \rangle \partial U/\partial y$, the only non-zero one in a boundary

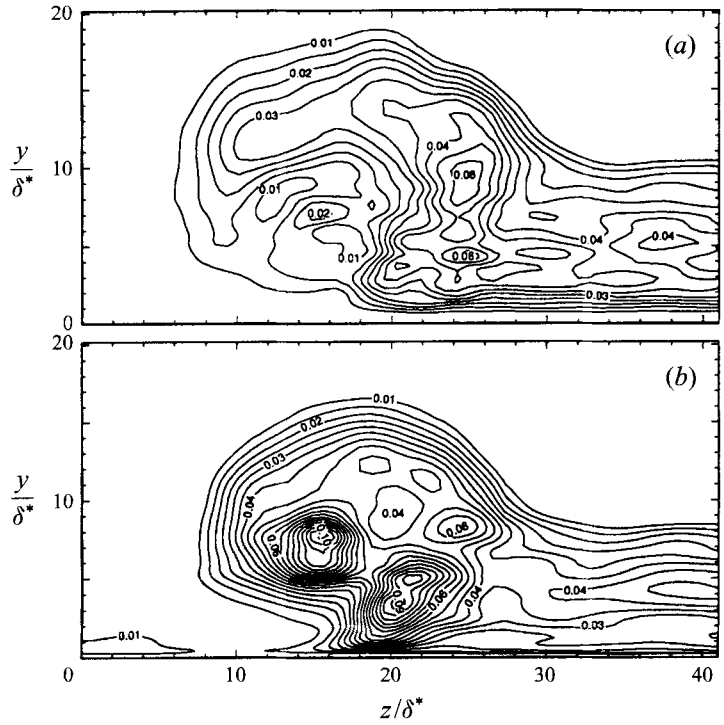

FIGURE 16. Contours of the eddy-viscosity at the second streamwise station. (*a*) ν_e from least-squares fit to LES results; (*b*) $\nu_e = C_\mu K^2/\epsilon$.

layer, dominates the region close to the wall and is almost spanwise-independent. The other significant production term, $-\langle u'w'\rangle \partial U/\partial z$, is only active in the immediate upwash region. Its location and shape are similar to the tongue of turbulent kinetic energy shown in figure 10, and it dominates all the other terms in the budget in this region, indicating that it is largely responsible for the generation of these high levels of energy. The production contributed by the normal stresses and the corresponding mean gradients, $-\langle v'^2\rangle \partial V/\partial y - \langle w'^2\rangle \partial W/\partial z$ (not shown), is negligible except in a small area in the immediate upwash region close to the wall, and its maximum value is much lower than those of the two dominant terms. The contribution of $-\langle v'w'\rangle \left(\partial V/\partial z + \partial W/\partial y\right)$ is also negligible. The contribution of the subgrid-scale stresses to the energy production, $\langle \tau_{ij}\rangle \langle \overline{S}_{ij}\rangle$, is about 10% of the total, and is confined to a very thin layer close to the wall ($y < 0.5\delta^*$). Similar to the two-dimensional boundary layer, the total production is significant in the near-wall region only. Since the production is negligible in the vortex core, the velocity gradient due to the momentum deficit in the core is not directly responsible for the high levels of turbulent kinetic energy shown in figure 10.

The dissipation of large-scale kinetic energy is shown in figure 18, which also includes the contribution of the subgrid-scale stresses. Again, this distribution is similar to that of a two-dimensional boundary layer except in the immediate upwash region, where the secondary flow convects the wall-layer turbulence away from the wall. The dissipation is lower than the production in the region around the vortex. The contribution of the subgrid-scale stresses, $\langle \tau_{ij}\overline{S}_{ij}\rangle$, is about 30% of the total, and is confined to a layer of thickness δ^*.

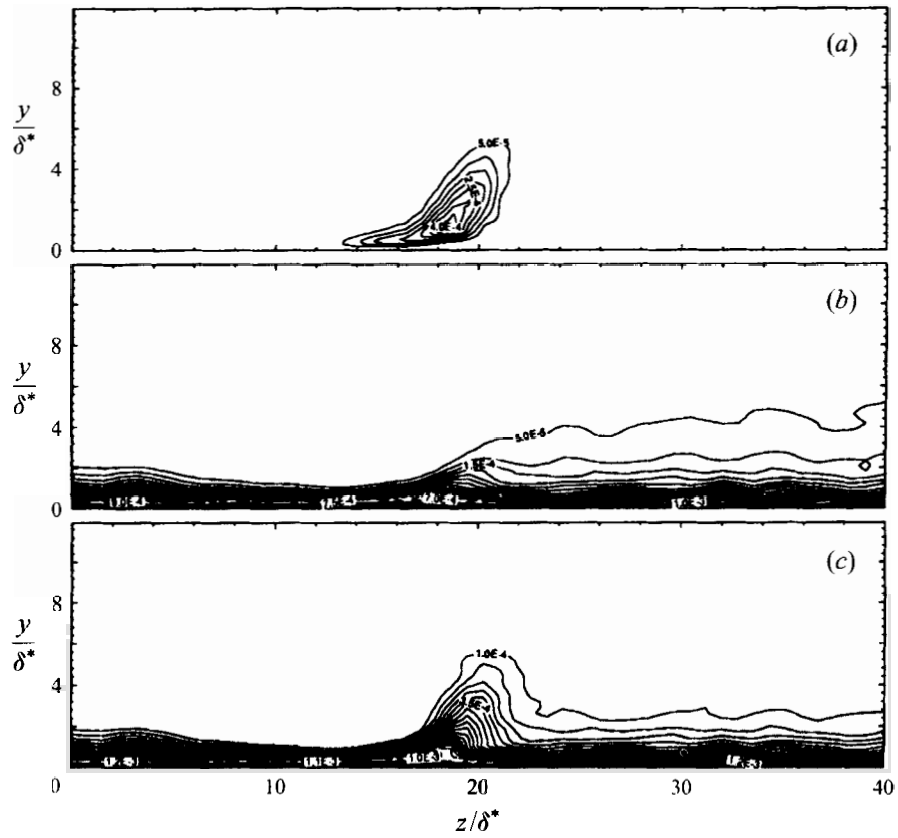

FIGURE 17. Contours of the production of turbulent kinetic energy at the second streamwise station. (*a*) $-\langle u'w'\rangle \partial U/\partial z$, (*b*) $-\langle u'v'\rangle \partial U/\partial y$, (*c*) total.

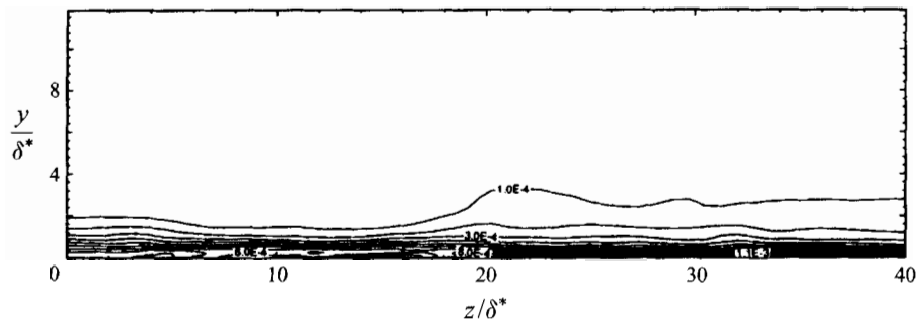

FIGURE 18. Contours of the dissipation at the second streamwise station.

The turbulent diffusion is shown in figure 19. In the upwash region, the turbulent transport $-\partial \langle u_i' u_k' u_k'/2\rangle / \partial x_i$, shown in figure 19(*b*), dominates the turbulent diffusion. The contours indicate that turbulent transport diffuses energy from the immediate upwash region towards the vortex core, increasing the kinetic energy there. However, near the vortex centre, the pressure diffusion is dominant, as shown in figure 19(*a*).

To visualize more clearly the turbulent transport process, the turbulent transport

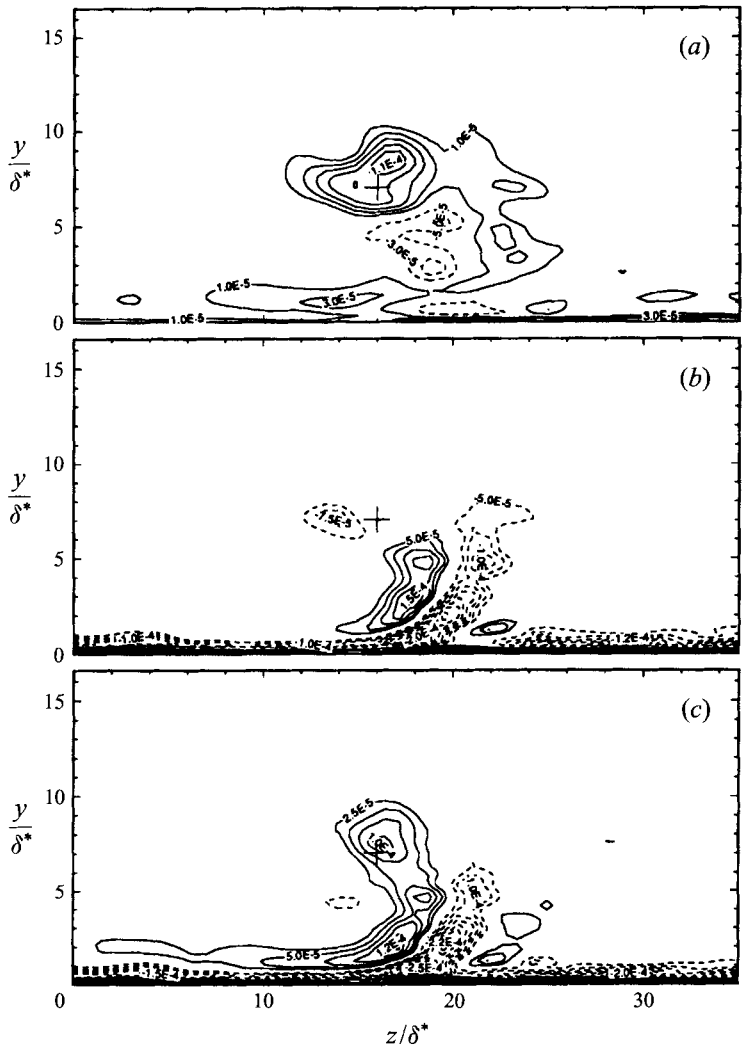

FIGURE 19. Contours of the turbulent diffusion of turbulent kinetic energy at the second streamwise station. A cross denotes the location of the vortex centre. (*a*) $-\partial \langle p'u_i' \rangle / \partial x_i$, (*b*) $-\partial \langle u_k' u_k' u_i'/2 \rangle / \partial x_i$, (*c*) total.

velocities of K can be defined, following Shabaka *et al.* (1985), as

$$V_q = \frac{\langle u_k' u_k' v' \rangle}{2K}, \quad W_q = \frac{\langle u_k' u_k' w' \rangle}{2K}; \tag{6.3}$$

their vector field is shown in figure 20, superimposed on the distribution of turbulent kinetic energy. Outside the vortex core, the vectors generally are aligned with the gradients of the turbulent kinetic energy, and diffuse energy away from the vortex region. Significant turbulent transport can be observed carrying energy from the immediate upwash region towards the surrounding area, especially towards the vortex core. In the vortex core region, however, the vectors do not align with the turbulent kinetic energy gradient; rather, they only spread energy around the vortex core, in agreement with the observations of Pauley & Eaton (1988*a*).

In $K - \epsilon$ modelling, the turbulent transport term is parameterized by a gradient

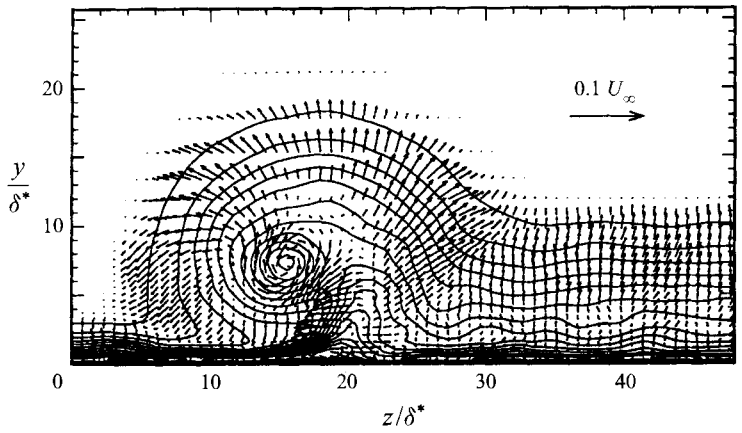

FIGURE 20. Turbulent transport velocity vectors for K, superimposed on the contours of K at the second streamwise station.

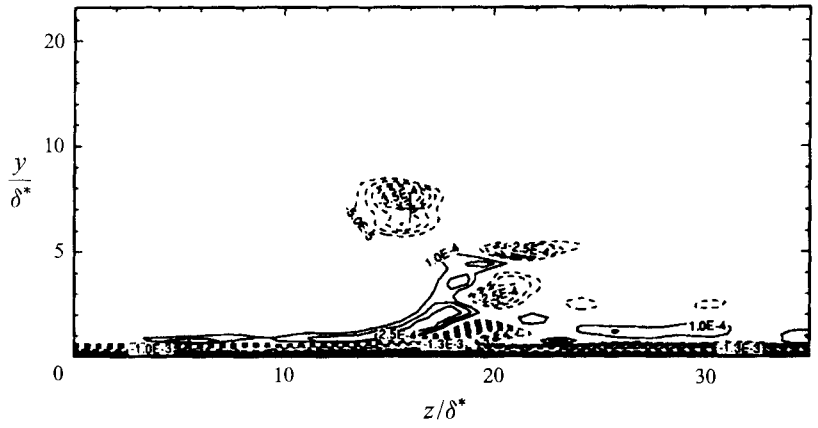

FIGURE 21. Contours of modelled turbulent diffusion at the second streamwise station. A cross denotes the location of the vortex centre.

transport hypothesis:

$$-\left\langle \frac{u_k' u_k' u_i' + p' u_i'}{2} \right\rangle = \frac{\nu_e}{\sigma_K} \frac{\partial K}{\partial x_i}, \tag{6.4}$$

where σ_K is a dimensionless constant. Based on the results shown in figure 20 the gradient-transport hypothesis is not expected to be very accurate inside the vortex. To elucidate this point further, the right-hand side of (6.4) has been evaluated using the present LES data and is shown in figure 21 (with $\nu_e = C_\mu K^2/\epsilon$). Figures 19(*c*) and 21 show a similar pattern in the upwash region, but the magnitude of the diffusion predicted by (6.4) is much higher than the value shown in figure 19. In the vortex core, the model prediction has the wrong sign altogether.

The transport equations of the large-scale Reynolds stresses R_{ij} are

$$\frac{\partial R_{ij}}{\partial t} + U_k \frac{\partial R_{ij}}{\partial x_k} = \mathscr{P}_{ij} - \mathscr{E}_{ij} + \Pi_{ij} - \frac{\partial C_{ijk}}{\partial x_k} + \nu \frac{\partial^2 R_{ij}}{\partial x_k \partial x_k}, \tag{6.5}$$

where

$$\mathscr{P}_{ij} = -R_{ik}\frac{\partial U_j}{\partial x_k} - R_{jk}\frac{\partial U_i}{\partial x_k} - \langle \tau_{ik}\rangle \frac{\partial U_j}{\partial x_k} - \langle \tau_{jk}\rangle \frac{\partial U_i}{\partial x_k}, \tag{6.6}$$

$$\mathscr{E}_{ij} = 2\nu \left\langle \frac{\partial u_i'}{\partial x_k}\frac{\partial u_j'}{\partial x_k}\right\rangle - \left\langle \tau_{jk}\frac{\partial \bar{u}_i}{\partial x_k}\right\rangle - \left\langle \tau_{ik}\frac{\partial \bar{u}_j}{\partial x_k}\right\rangle, \tag{6.7}$$

$$\Pi_{ij} = \left\langle p'\left(\frac{\partial u_i'}{\partial x_j} + \frac{\partial u_j'}{\partial x_i}\right)\right\rangle, \tag{6.8}$$

$$C_{ijk} = \langle u_i' u_j' u_k' + p' u_i' \delta_{jk} + p' u_j' \delta_{ik} + \tau_{jk}' u_i' + \tau_{ik}' u_j'\rangle \tag{6.9}$$

are the production, dissipation, pressure–strain correlation, and third-order diffusion correlation, respectively (Speziale 1991). In the following discussion, only the budgets for the primary shear stress $-\langle u'v'\rangle$ will be shown in detail. Some comments regarding the other components will be made at the end of the section.

The large-scale contribution to the production of $-\langle u'v'\rangle$, if the streamwise gradients are neglected, can be written as

$$R_{1k}\frac{\partial V}{\partial x_k} + R_{2k}\frac{\partial U}{\partial x_k} \simeq \langle v'^2\rangle \frac{\partial U}{\partial y} - \langle u'v'\rangle \frac{\partial W}{\partial z} + \langle u'w'\rangle \frac{\partial V}{\partial z} + \langle v'w'\rangle \frac{\partial U}{\partial z}. \tag{6.10}$$

In addition to $\langle v'^2\rangle \partial U/\partial y$, the only non-zero production term in a two-dimensional boundary layer, the three spanwise gradients of the mean velocities all contribute to the production of the primary shear stress through the corresponding shear stresses.

The contribution of the terms that are strictly due to the three-dimensionality of the flow is shown in figure 22(*a*). As in the boundary layer, the total production, shown in figure 22(*c*), is dominated by $\langle v'^2\rangle \partial U/\partial y$, especially close to the wall; however, this production term is drastically distorted in the vortex region by the secondary flow. As expected, the three-dimensional terms are only significant in the vortex region, and they are smaller than, and usually of opposite sign to $\langle v'^2\rangle \partial U/\partial y$. Outside the vortex core, the distribution of the total production shows a pattern similar to that of $-\langle u'v'\rangle$ (see figure 13), whereas, inside the core it does not. In addition, the magnitude of the total production in the vortex core is not small, indicating that the mean gradient effects are important for the generation of $-\langle u'v'\rangle$, although they are negligible in the generation of turbulent kinetic energy in the vortex core.

The pressure–strain correlation Π_{12} is shown in figure 23. Outside the vortex core, this term is generally of opposite sign to the production, in agreement with the results observed in a DNS of a two-dimensional turbulent boundary layer (Spalart 1988). Inside the core, on the other hand, it shows a pattern similar to the production but with lower magnitude.

The third-order diffusion correlation is of the form

$$\frac{\partial C_{12k}}{\partial x_k} = \frac{\partial}{\partial y}\langle u'v'v' + p'u'\rangle + \frac{\partial}{\partial z}\langle u'v'w'\rangle, \tag{6.11}$$

and is shown in figure 24. The pressure term is the dominant one in this case. Outside the near-wall region, it is only significant in the vortex core, where it has a slightly larger magnitude than that of the pressure–strain correlation. The contribution of $\partial\langle p'u'\rangle/\partial y$ cannot be neglected in this type of three-dimensional turbulent flow.

Figure 25 shows the transport velocities of $-\langle u'v'\rangle$, defined as

$$V_{uv} = \frac{\langle u'v'v'\rangle}{\langle u'v'\rangle}, \quad W_{uv} = \frac{\langle u'v'w'\rangle}{\langle u'v'\rangle}, \tag{6.12}$$

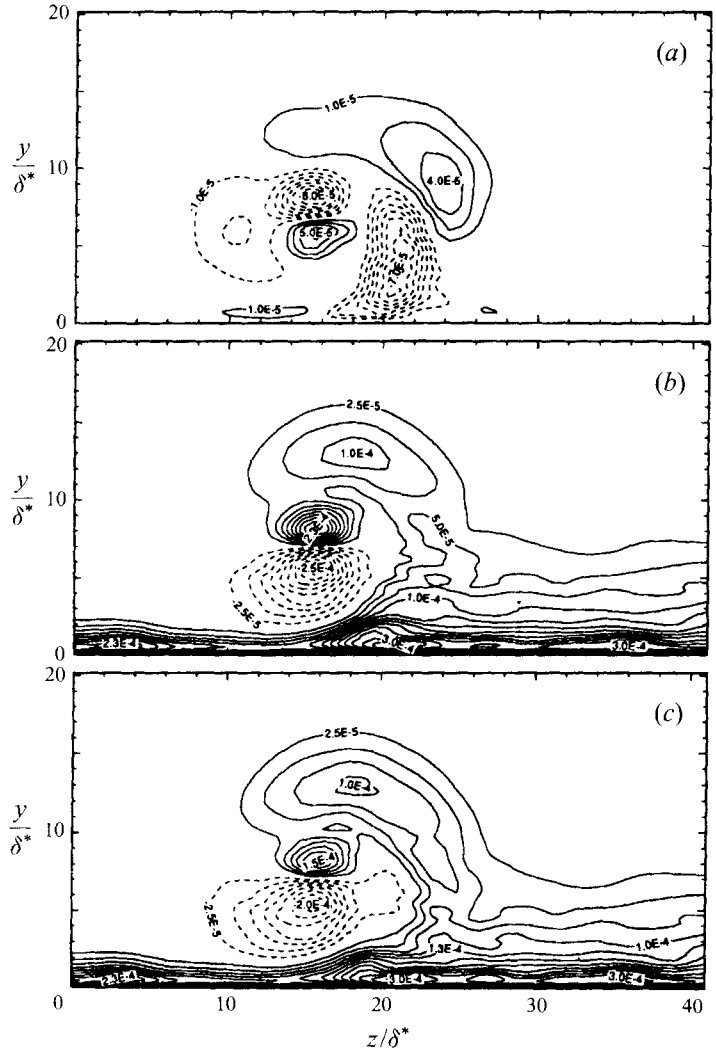

FIGURE 22. Contours of the production of $-\langle u'v'\rangle$ at the second streamwise station. (*a*) $-\langle u'v'\rangle\partial W/\partial z + \langle u'w'\rangle\partial V/\partial z + \langle v'w'\rangle\partial U/\partial z$, (*b*) $\langle v'^2\rangle\partial U/\partial y$, (*c*) total large-scale production.

superimposed on the distribution of $-\langle u'v'\rangle$. In the region away from the vortex core, the vectors generally are aligned with the gradients of $-\langle u'v'\rangle$, but the magnitudes are not strongly correlated. In the vortex core, neither direction nor magnitude are correlated. Turbulent transport from the immediate upwash region to the vortex core is smaller than for the turbulent kinetic energy, shown in figure 20. In general, however, the magnitude of this transport velocity is larger than that of the turbulent kinetic energy transport velocities shown in figure 20.

The results of the transport analysis of the two secondary shear stresses are not shown here. The pressure-strain correlations of these stresses are also generally opposite to their production, and the third-order diffusion correlations are significant in the vortex core region. The dissipation rates are negligible.

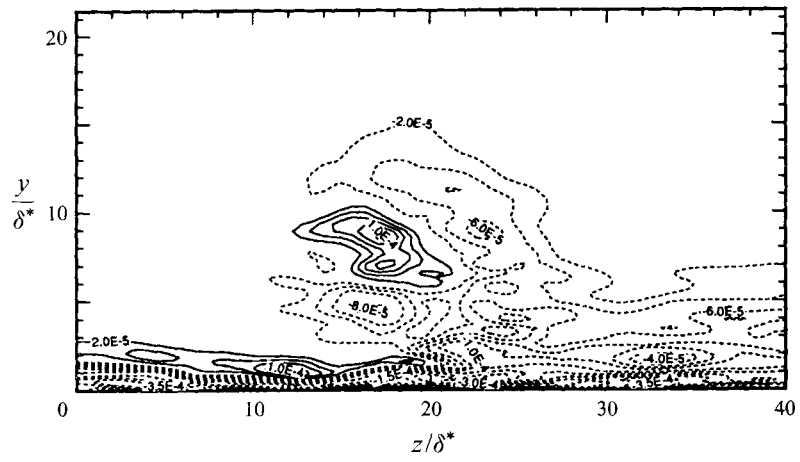

FIGURE 23. Pressure–strain correlation Π_{12}.

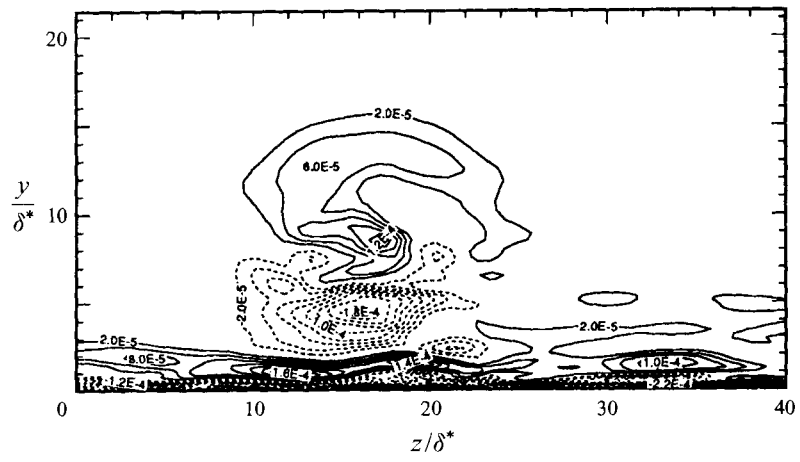

FIGURE 24. Third-order correlation $\partial C_{12k}/\partial x_k$.

7. Conclusion

The interaction between a zero-pressure-gradient turbulent boundary layer and a pair of strong embedded common-flow-down streamwise vortices was studied by large-eddy simulation. The agreement with experimental data was generally good, in spite of differences in the vortex generation and in the Reynolds number. This calculation is part of a trend of studies in which LES is applied to more complex flows with increased technological impact. This study will be extended to co-rotating vortex generators.

The vortices are generated by body forces. An Oseen vortex generator is proposed, along with a wake generator to account for the velocity deficit introduced by the actual delta-wing vortex generators used in experiments. The velocity profiles of the vortices agree well with those of the Oseen vortex and the experimental data.

The embedded vortices drastically distort the boundary layer by downwash and upwash over great streamwise distance. The velocity profiles deviate significantly from the undisturbed profile, close to the vortex. In addition, secondary vorticity with

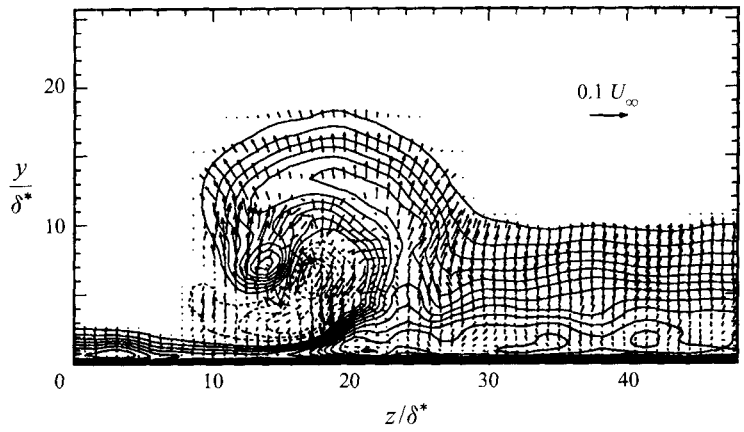

FIGURE 25. Turbulent transport velocity vectors for $-\langle u'v' \rangle$, superimposed on the contours of $-\langle u'v' \rangle$ at the second streamwise station.

opposite sign to the embedded vorticity is observed close to the wall and rolled up by the secondary flow in the upwash region. The embedded vortices produce a large spanwise variation of the skin friction and introduce spanwise skin friction in the vortex region.

The Reynolds stresses are significantly modified and become three-dimensional. The secondary flow due to the vortices confines the turbulence to a thin layer in the downwash region and suppresses it by straining. Conversely, high levels of turbulent kinetic energy and anisotropy of the normal stresses are observed in the upwash region. The two secondary Reynolds stresses are also significant there. In the vortex core, high levels of turbulent kinetic energy and negative shear stress $-\langle u'v' \rangle$ are observed.

Production and dissipation of kinetic energy are relatively low in the core, while the interaction between the pressure and the velocity fluctuations is strong and is the primary mechanism responsible for the high energy levels. The pressure–strain correlations for the shear stresses are generally opposite to the productions except the vortex core region, where the pressure–strain correlation of the primary shear stress has the same sign as the production. Turbulent transport from the immediate upwash region is an important mechanism for the turbulent kinetic energy, less so for $-\langle u'v' \rangle$.

Modelling the diffusion term by a gradient transport hypothesis leads to significant errors in the vortex core. A scalar eddy viscosity cannot be fully accurate in this type of three-dimensional flow; the distribution of $C_\mu K^2/\epsilon$ is different from any 'eddy viscosity' constructed from the strain and stress tensors. It gives a large value at the vortex centre, resulting in the excessively fast decay of the streamwise vorticity in $K-\epsilon$ model calculations. The complex behaviour of the pressure-strain correlation and similar terms in the vortex region would probably make even Reynolds-stress modelling difficult to apply in this type of flow.

This research was sponsored by the Office of Naval Research, and monitored by Dr L. Patrick Purtell. The computations were performed at the Pittsburgh Supercomputing Center. The authors thank Dr Wayne R. Pauley who kindly gave permission to use his data.

REFERENCES

ANDERSON, S. D., EATON, J. K. 1987 An experimental investigation of pressure driven three-dimensional turbulent boundary layers. *Rep.* MD-49. Thermosciences Div., Dept. Mech. Eng., Stanford University.

ANTONIA, R. A., SPALART, P. R. & MARIANI, P. 1994 Effect of suction on the near-wall anisotropy of a turbulent boundary layer. *Phys. Fluids* **6**, 430–432.

BRADSHAW, P. 1987 Turbulent secondary flows. *Ann. Rev. Fluid Mech.* **19**, 53–74.

CABOT, W. H. & MOIN, P. 1993 Large eddy simulation of scalar transport with the dynamic subgrid-scale model. In *Large Eddy Simulation of Complex Engineering and Geophysical Flows* (ed. B. Galperin & S.A. Orszag), pp. 141–158. Cambridge University Press.

CUTLER, A. & BRADSHAW, P. 1989 Vortex/boundary-layer interactions. *AIAA Paper* 89-0083.

EIBECK, P. A. & EATON, J. K. 1985 An experimental investigation of the heat-transfer effects of a longitudinal vortex embedded in a turbulent boundary layer. *Rep.* MD-48. Thermosciences Div., Dept. Mech. Eng., Stanford University.

ESMAILI, H. 1992 Large-eddy simulation of temporally developing boundary layers with embedded streamwise vortices. PhD thesis, University of Maryland, College Park.

ESMAILI, H. & PIOMELLI, U. 1992 Temporal development of turbulent boundary layers with embedded streamwise vortices. *Theor. Comput. Fluid Dyn.* **6**, 369–380.

FONTAINE, A. A., BIENIEWSKI, S. & DEUTSCH, S. 1993 Turbulent boundary layer modification by generation of counter-rotating vortices within the buffer region. In *Near-Wall Turbulent Flows* (ed. R. M. C. So, C. G. Speziale & B. E. Launder), pp. 467–476. Elsevier.

GERMANO, M. 1992 Turbulence: the filtering approach. *J. Fluid Mech.* **238**, 325–336.

GERMANO, M., PIOMELLI, U., MOIN, P. & CABOT, W.H. 1991 A dynamic subgrid-scale eddy viscosity model. *Phys. Fluids* A **3**, 1760–1765.

GHOSAL, S., LUND, T. S., MOIN, P. & AKSELVOLL, K. 1995 A dynamic localization model for large-eddy simulation of turbulent flows. *J. Fluid Mech.* **286**, 229–255.

KIM, W. J. & PATEL, V. C. 1994 Influence of streamwise curvature on longitudinal vortices imbedded in turbulent boundary layers. *Computers & Fluids* **23**, 647–673.

LIANDRAT, J., AUPOIX, B. & COUSTEIX, J. 1987 Calculation of longitudinal vortices embedded in a turbulent boundary layer. In *Turbulent Shear Flows 5* (ed. F. Durst *et al.*), pp. 253–265. Springer.

LILLY, D. K. 1992 A proposed modification of the Germano subgrid-scale closure method. *Phys. Fluids* A **4**, 633–635.

LIU, J. 1994 Interaction between a spatially growing turbulent boundary layer and embedded streamwise vortices. PhD thesis, University of Maryland, College Park.

LUND, T., GHOSAL, S., & MOIN, P. 1993 Numerical experiments with highly-variable eddy viscosity models. In *Engineering Application of Large Eddy Simulations – 1993* (ed. S. A. Ragab & U. Piomelli). The Fluids Engineering Division, ASME.

MATSUMOTO, A. 1986 Turbulent boundary layer perturbed by streamwise vortices. *J. Japan Soc. Aero. Space Sci.* **34**, 141–152.

MEHTA, R. D. & BRADSHAW, P. 1988 Longitudinal vortices embedded in turbulent boundary layers. Part 2. Vortex pair with 'common flow' upwards. *J. Fluid Mech.* **188**, 529–546.

PAULEY, W. R. & EATON, J. K. 1988*a* The fluid dynamics and heat transfer effects of streamwise vortices embedded in a turbulent boundary layer. *Rep.* MD-51. Thermosciences Div., Dept. Mech. Engng, Stanford University.

PAULEY, W. R. & EATON, J. K. 1988*b* Experimental study of the development of longitudinal vortex pairs embedded in a turbulent boundary layer. *AIAA J.* **26**, 816–823.

PHILLIPS, W. R. C. & GRAHAM, J. A. H. 1984 Reynolds-stress measurements in a turbulent trailing vortex. *J. Fluid Mech.* **147**, 353–371.

SANKARAN, L. & RUSSELL, D. A. 1990 A numerical study of longitudinal vortex interaction with a boundary layer. *AIAA Paper* 90-1630.

SENDSTAD, O. & MOIN, P. 1992 The near wall mechanics of three-dimensional turbulent boundary layers. *Rep.* TF-57. Thermosciences Div., Dept. Mech. Eng., Stanford University.

SHABAKA, I. M. M. A., MEHTA, R. D. & BRADSHAW, P. 1985 Longitudinal vortices embedded in turbulent boundary layers. Part 1. Single vortex. *J. Fluid Mech.* **155**, 37–57.

SHIZAWA, T. & EATON, J. K. 1992 Interaction of a longitudinal vortex with a three-dimensional, turbulent boundary layer. *AIAA J.* **30**, 1180–1181.

SPALART, P. R. 1988 Direct numerical simulation of a turbulent boundary layer up to $Re_\theta = 1410$. *J. Fluid Mech.* **187**, 61–98.

SPALART, P. R. 1989 Theoretical and numerical study of a three-dimensional turbulent boundary layer *J. Fluid Mech.* **205**, 319–340.

SPALART, P. R. & WATMUFF, J. H. 1993 Experimental and numerical study of a turbulent boundary layer with pressure gradients. *J. Fluid Mech.* **249**, 337–371.

SPEZIALE, C. G. 1991 Analytical methods for the development of Reynolds-stress closures in turbulence. *Ann. Rev. Fluid Mech.* **23**, 107–157.

TAKAGI, S. & SATO, H. 1983 An experiment on the interation of a turbulent boundary layer and a row of longitudianl vortices. *J. Japan Soc. Fluid Mech.*, **2**, 288–300.

WENDT, B. J., GREBER, I. & HINGST, W. R. 1992 The structure and development of streamwise vortex arrays embedded in a turbulent boundary layer. *AIAA Paper* 92-0551.

WESTPHAL, R. V., EATON, J. K. & PAULEY, W. R. 1985 Interaction between a vortex and a turbulent boundary layer in a streamwise pressure gradient. In *Proc. Fifth Symposium on Turbulent Shear Flows, Ithaca, NY.*

ZANG, T. A. & HUSSAINI, M. Y. 1988 Numerical experiments on the stability of controlled boundary layers. *ICASE Rep.* 88-20. ICASE–NASA Langley Research Center.